CdZnTe Detectors Operating at X-ray Fluxes of 100 Million Photons/(mm^{2}·sec)

Michael Prokesch, Stephen A. Soldner, Arunmozhi G. Sundaram, Michael D. Reed, Handong Li, John F. Eger, Jaqueline L. Reiber, Carrie L. Shanor, Corey L. Wray, Aaron J. Emerick, Alan F. Peters, and Corey L. Jones

***Abstract*— CdZnTe single crystals grown with the traveling heater method have been specifically engineered to support high-flux x-ray photon counting applications. Pixelated detector devices absorb hardened 120 kV_p fluxes up to 10^8 photons/(mm^2·sec) without any sign of electric field polarization at room temperature (23-28) °C. It is shown that detector functionality can be verified using photon counting electronics even under conditions of strong pulse pile-up. A non-paralyzable counting model satisfactory describes the average output count rate of the detector-electronics system as a function of the absorbed flux. Good pixel-to-pixel count rate uniformity can be achieved.**

***Index Terms*— ASIC, Cd-based compound semiconductors, CdZnTe, high-flux, photon counting, pile-up, polarization, traveling heater, x-ray detectors.**

I. Introduction

CdZnTe (CZT) and CdTe are currently considered the semiconductor materials of choice for high-efficiency, energy-resolved high-flux x-ray photon counting applications like medical computed tomography (spectral CT) or security applications like baggage screening [1]–[7].

Various melt-, solvent- and vapor phase crystal growth techniques have been employed over the years to produce CZT and CdTe single crystals with improved electrical and structural properties [8]–[10].

We have extensively employed several variants of the Bridgman technique including the high-pressure electrodynamic gradient method (HP-EDG) and more recently, the solvent based traveling heater method (THM), in which the ingots crystallize out of a solution well below the congruent melting point [11].

With respect to the charge transport properties of the semi-insulating material, the smallest variations of the crystal defect structure, and in particular native point defect concentrations, can render the semiconductor more or less suitable for different application types [12]. High resolution spectroscopy/imaging with pixelated detectors, for instance, requires material with high electron-mobility lifetime product and uniformity, while high-flux photon counting applications demand good hole transport to avoid excessive space charge build-up under intense x-ray radiation. Other requirements for the latter are fast temporal response and a high achievable charge sweep-out speed. This work is focused on the demonstration of the high-flux counting capabilities of our THM grown CZT.

Manuscript received February 8, 2016; revised March 30, 2016; accepted April 16, 2016. Date of current version June 21, 2016.

The authors are with eV Products Inc., Saxonburg, PA 16056 USA (e-mail: Michael.Prokesch@evproducts.com; Steve.Soldner@evproducts.com; arunmozhi.sundaram@evproducts.com; drmichaelreed@hotmail.com; handong.li@gmail.com; John.Eger@evproducts.com; jackie.reiber@evproducts.com; Carrie.Shanor@evproducts.com; corey.wray@evproducts.com; aaron.emerick@evproducts.com; alan.peters@evproducts.com; Corey.Jones@evproducts.com).

Color versions of one or more of the figures in this paper are available online at http://ieeexplore.ieee.org.

Digital Object Identifier 10.1109/TNS.2016.2556318

II. Detector and Electronics Challenges

A typical sensor configuration consists of a biased, low background carrier concentration semiconductor detector with pixelated anode and a read-out circuitry comprised of charge sensitive pre-amplifiers and analog pulse shaping filter stages at the front-end.

Hence, one basic requirement for those applications is a fast resetting signal shaping electronics with short peaking times to push out the pile-up limitation when the frequency of absorbed photons with energies above threshold Φ_{abs} per read-out channel detection area A_D approaches the inverse resolution time (effective dead time τ_{eff}) of the pulse counting chain:

$$\Phi_{abs} A_D \rightarrow \tau_{eff}^{-1}. \tag{1}$$

Another requirement for counting with conventional signal chains is the fast collection of the photo-generated charge clouds to facilitate their separation, i.e., high sensor or charge sweep-out speed. This becomes critical when $\Phi_{abs} A_D$ approaches the inverse average transit time of the photo-generated electrons to the anode pixels. Assuming non-degeneration of the internal electric field, this can be expressed as a minimum bias $V_{\min}$ that needs to be applied to the detector:

$$V_{\min} \sim \Phi_{abs} A_D \left(\frac{d-1}{\lambda_E}\right) \frac{d}{\mu_e}, \tag{2}$$

where d is the detector thickness, λ_E is the x-ray energy dependent linear attenuation coefficient, i.e., the inverse of mean free path or absorption depth and μ_e is the electron drift mobility.

Given the limited drift mobility of the photo-generated electrons in the conduction band and the insignificant temperature dependence of this parameter in technically relevant temperature ranges, the semiconductor sensor speed can only be increased by reducing the detector thickness, increasing the bias voltage or shortening the effective induction distance

(side irradiation, smaller pixels, etc.). However, those approaches constitute trade-offs with respect to detection efficiency, dark leakage current, noise and charge sharing. Reducing the active sensor area per ASIC read-out channel, for instance, can help to reduce the rate of counts to be effectively handled at a given incident flux density, however, this approach is limited by charge sharing effects if the size of the anode pixel pitch becomes small enough for a significant fraction of charge clouds to be shared between multiple pixels.

Arguably, the most fundamental technological challenge from a semiconductor materials development standpoint is to prevent high-flux polarization [13]. This effect is caused by excessive space charge build-up due to trapping of photo-generated holes under intense x-ray irradiation causing dynamic, i.e., reversibly flux dependent collapse of the internal electric field [13]–[15]. This can increase the average transit time of the electron clouds beyond the effective peaking time of the shaping electronics. In this situation, pulses are recorded with reduced amplitudes (ballistic deficit) and as the flux further increases, the entire pulse height spectrum can shift gradually below the counting thresholds. The overall count rate will effectively decrease with further increasing photon flux and eventually vanish completely. Pile-up effects due to increasing photon arrival frequency and slowing transients due to space charge can convolute with this trend.

Note, that this radiation induced polarization mechanism must not be confused with the long time scale, bias induced (dark) polarization as observed, e.g., on slightly p-type CdTe Schottky-type detectors, which is due to negative space charge build up underneath the blocking anode contact [16], [17].

Besides operational parameters like bias and temperature, which affect the overall hole transport (drift velocity in the valence band and detrapping rates), the mobility-lifetime product of the photo-generated holes is the single most critical materials parameter that determines if the detector will catastrophically polarize above some critical x-ray flux or stay functional for high-flux counting. Hence, the first challenge of CZT development from low-flux spectroscopy/imaging optimized materials towards CZT for high-flux x-ray applications is the controlled modification of the crystals defect structure.

III. Experimental Details

The detectors investigated in this study were fabricated from CZT ingots grown with the THM at eV Products. The crystal growth processes were modified to achieve improved hole transport in the crystals. Typical values of the achieved hole mobility-lifetime product as determined from alpha gain measurements on quasi-planar devices are now in the range of $(1-7)\times 10^{-5}$ cm^2/V at room temperature. Though the absolute accuracy of this test may be somewhat limited given the still relatively weak charge signals this is about one order of magnitude up from our low-flux spectroscopy/imaging optimized CZT.

The monolithic test devices are 3 mm thick and feature 16×16 anode pixel arrays at a pitch of 0.5 mm. The counting system is based on the eV-230B ASIC, which is an 8-channel

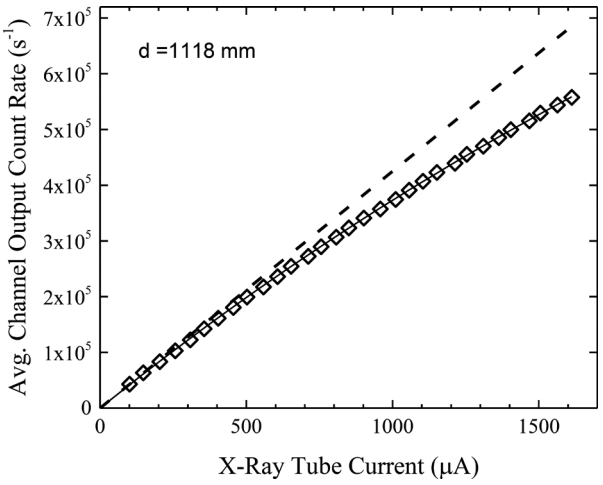

Fig. 1. Channel output count rate as a function of x-ray tube current at 1,118 mm distance. All 256 pixel count rates are averaged for each tube current (diamonds). Each channel covers 0.25 mm^2 detector area. The dashed line is the linear approximation and the solid line connecting the data points is a fit according to (4).

device with active leakage current compensation and bi-polar shaping amplifier circuitry with ∼ 150 ns peaking time as determined from low-flux shaper output[1] and a single energy threshold which was set to 30 keV. The 256 pixel probe test, measurement electronics and data acquisition system were described in detail elsewhere [18]. The test system was placed in a 120 kV$_p$ x-ray beam hardened by a 1 mm thick brass filter resulting in a mean photon energy of ∼75 keV, which gives a mean free path for the x-ray photons of ∼0.5 mm underneath the cathode. All x-ray measurements were carried out at nominally room temperature with some minor warm-up of the test box at longer operation (23-28) °C.

IV. Flux Calibration

The incident x-ray flux was estimated using the detector-readout system itself: The detector was placed at a larger distance (>1 m) from the x-ray source, which was then ramped through a sequence of tube currents. The absorbed photon flux was estimated from the lowest flux levels for which the channel output count rate is about proportional to the flux, which in turn is proportional to the tube current. This is shown in figure Fig. 1.

Using the low-flux proportionality constant c as obtained at distance d_{cal} and assuming a quadratic dependence of the absorbed flux Φ_{abs} on the x-ray target-to-detector distance, the absorbed flux at any distance d and tube current I_{tube} can be estimated to:

$$\Phi_{abs} \sim c I_{tube} \frac{{d_{cal}}^2}{d^2}. \tag{3}$$

Note that without a calibrated reference system, a more accurate determination of the incident flux can become relatively involved even at very low flux and without count loss due to ballistic deficit. For our specific detector geometry,

[1]In [18], a peaking time of 190 ns was quoted from the ASIC data sheet.

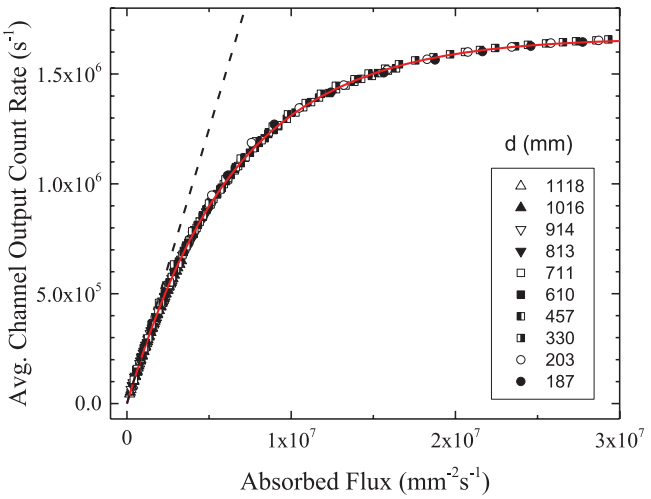

Fig. 2. Average channel output count rates as a function of the absorbed flux (symbol sets). The data are compiled from the individual 256 channel count rates for 31 tube current steps at each of 10 different target-to-detector distances. Fit according to (4) (solid line) and pile-up correction according to (5) (dashed line).

single low energy threshold and hardened incident x-ray spectral distribution, charge sharing effects should lead mostly to flux overestimates due to multiple counting (rather than count loss). Our energy threshold was set to 30 keV and the brass filter effectively removes low-energy photons from the incident x-ray spectrum ($< 0.1\%$ of primary photons below 36 keV). However, escape of fluorescence photons will still lead to charge deposition well below energy threshold despite the filter. This can lead to underestimates of the incoming flux while this "unaccounted" charge will still contribute to space charge build-up.

V. Output Count Rate Correction

With our measurement configuration, the highest attainable x-ray flux incident to the detector cathode is ~100 Mil. pps/mm^2.[2] At those flux levels, the average photon deposition rate is ~1 photon per channel every 40 ns (0.5 mm pixel pitch). This unavoidably leads to severe pile-up given the ~ 150 ns peaking time of the shaper and even longer effective dead time of the system. The latter can be expected to be in the range of the width of the bipolar pulses that was determined from the shaper output signals at low flux to be ~600 ns. In fact, the output count rate starts deviating from linearity already at fluxes below 1 Mil. pps/mm^2 (0.25 Mil. cps/channel) as can be seen in Fig. 1.

Fig. 2 shows the non-linear response of the counting system coupled to a non-polarizing THM detector for absorbed fluxes up to 30 Mil. pps/mm^2. The data points are the averaged count rates of all 256 individual pixels. Thirty-one different x-ray tube currents have been applied at each of ten different target-detector distances. The x-axis was re-calibrated for each distance according to (3). The perfect line up of the combined data sets proves the correctness of the assumptions made for the flux calibration.

[2]We use "Mil. pps/mm^2" to abbreviate "Million photons/(mm^2·sec)".

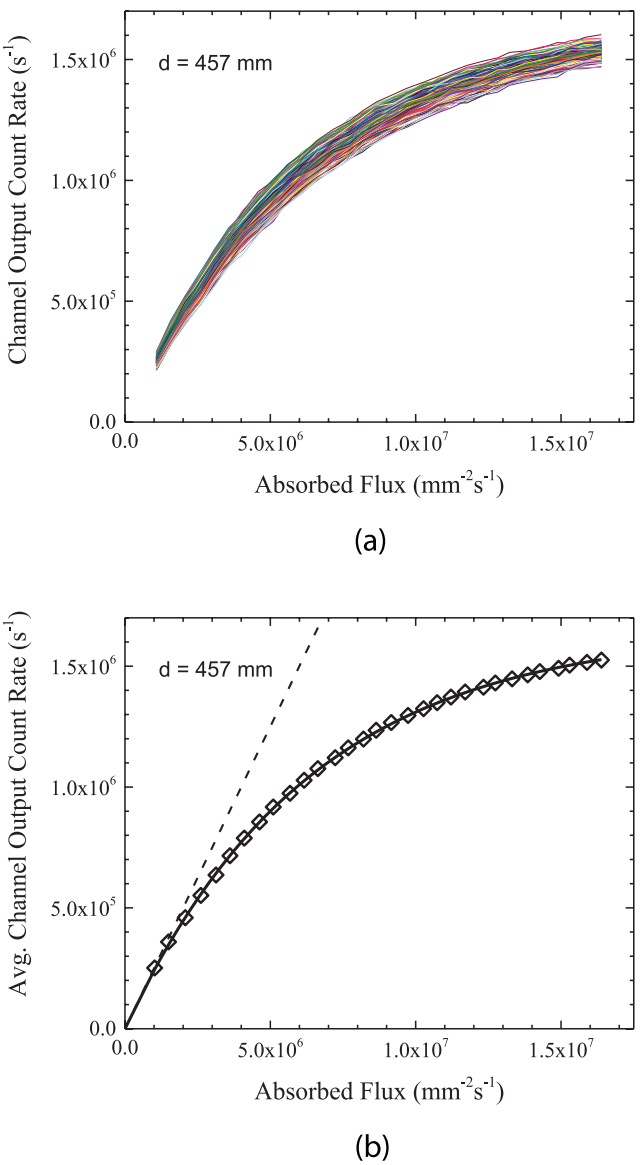

Fig. 3. (a) Output count rates from all 256 pixels at fixed 457 mm target-to-detector distance, and (b) Averaged count rates (diamonds), fit according to (4) (solid line) and pile-up correction according to (5) (dashed line).

This counting system can be described by a non-paralyzable, fixed dead-time model as outlined previously [19]. This time, we significantly extend the flux range and average the pixel counts to mitigate effects of potential flux-dependent charge steering on the response analysis [20]. The solid line in Fig. 2 shows the calculated ASIC channel output count rate C_{ch} as a function of the absorbed photon flux Φ_{abs} according to:

$$C_{ch}(\Phi_{abs}) \sim \tau_{eff}^{-1}[1 - \exp(-\tau_{eff}\kappa A_{eff}\Phi_{abs})]. \quad (4)$$

The major fitting parameter is the effective dead time τ_{eff} of the signal chain. A_{eff} is the effective pixel area, which is about the square of the pixel pitch in our case and κ is a dimensionless correction factor for the event rate in the detector, accounting for inaccuracies of the flux calibration, energy and charge losses, charge sharing related double counting, etc. This fit accurately describes the experimentally observed dependence in Fig. 2 for k = 1.03 and τ_{eff} = 600 ns.

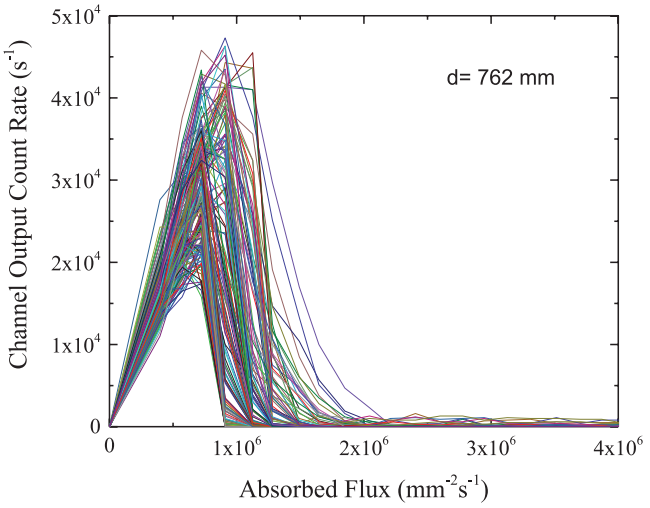

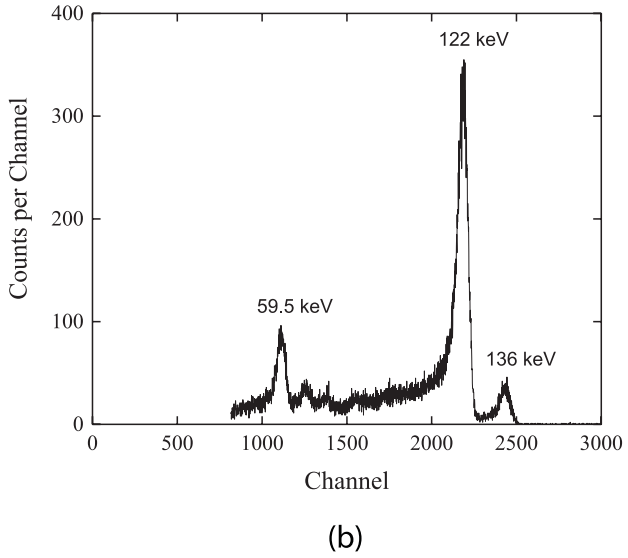

Fig. 4. (a) Flux dependence of the output count rates from the pixels of a polarizing test device made from a low-flux spectroscopy/imaging CZT crystal ingot at 900 V bias. Dead and outer pixels removed and zero point added for clarity. (b) Low-flux ^{241}Am +^{57}Co pixel spectrum from a 5 mm thick, 1.6 mm pixel pitch witness detector from the same ingot shows good spectroscopic performance at room temperature.

The pile-up correction for the output count rate as also plotted in Fig. 2 is straight forward:

$$C_{ch}^{cor}(\Phi_{abs}) \sim \frac{-\ln(1-\tau_{eff}C_{ch})}{(\tau_{eff}\kappa)}. \quad (5)$$

At higher fluxes, the output count rate according to (4) simply approaches the asymptotic value of the classical non-paralyzable model $C_{ch}(\infty) \sim \tau_{eff}^{-1}$ [19].

Fig. 3(a) shows the output count rates from all 256 pixels of the same detector at one fixed target-to-detector distance. Fig. 3(b) shows the averaged count rates, the counting model fit according to (4) and the pile-up corrected rates according to (5).

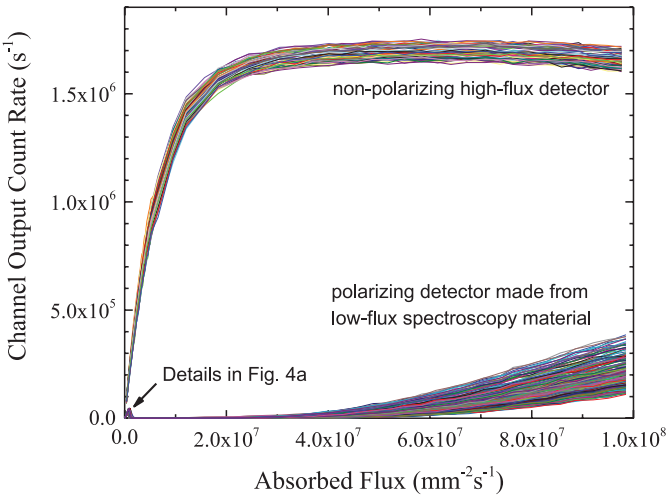

Fig. 5. Comparison of the channel output count rates with a non-polarizing and a polarizing detector at 900 V bias and room temperature for absorbed x-ray fluxes up to ~ 100 Mil. pps/mm^2. Dead and outer pixels removed for clarity.

VI. Tests at 100 Million Photons/(mm^{2}·sec)

While this acquisition electronics and specific detector configuration cannot be used for accurate photon counting much beyond 10 Mil. pps/mm^2, proper operation of the semiconductor detector itself can be still verified at absorbed flux levels up to 100 Mil. pps/mm^2, which is the maximum we can currently apply with the existing x-ray setup.

First, we verified the behavior of the counting system when a polarizing detector is connected to the front-end circuitry by preparing high-flux test devises (3 mm thick, 0.5 mm pitch) from a low-flux, spectroscopy/ imaging CZT crystal ingot. Fig. 4(a) shows the x-ray flux dependence of the output count rates of the pixels, which collapses above a critical flux of $<$ 1 Mil. pps/mm^2 at 900 V bias. The otherwise good spectroscopic capability of this crystal material was confirmed on separate witness samples (5 mm thick, 1.6 mm pitch) from the same crystal. Fig. 4(b) shows a low-flux ^{241}Am +^{57}Co pixel spectrum obtained with such a device [12]. This spectroscopy material has a relatively high electron mobility-lifetime product of $\sim 1 \times 10^{-2}$cm^2/V but the hole mobility-lifetime product is only $\sim 5 \times 10^{-6}$cm^2/V at room temperature, which makes the material prone to positive space charge accumulation and hence, polarization.

Fig. 5 shows the channel output count rates obtained with a non-polarizing high-flux detector at 900 V bias and room temperature for absorbed x-ray fluxes up to ~100 Mil. pps/mm^2. Due to limitations of the tube current settings, flux calibrated data sets from two different target-to-detector distances (813 mm and 187 mm) have been stitched together for this plot. This particular device is from a CZT crystal with a relatively low electron mobility-lifetime product of $\sim 1.5 \times 10^{-3}$cm^2/V but a higher hole mobility-lifetime product of $\sim 2 \times 10^{-5}$cm^2/V, which can obviously accommodate efficient back drift of the photo-generated holes to the cathode without any sign of polarization.

As predicted by (4), the average count rate saturates at ~1.65 Mil. cps/channel when the absorbed flux

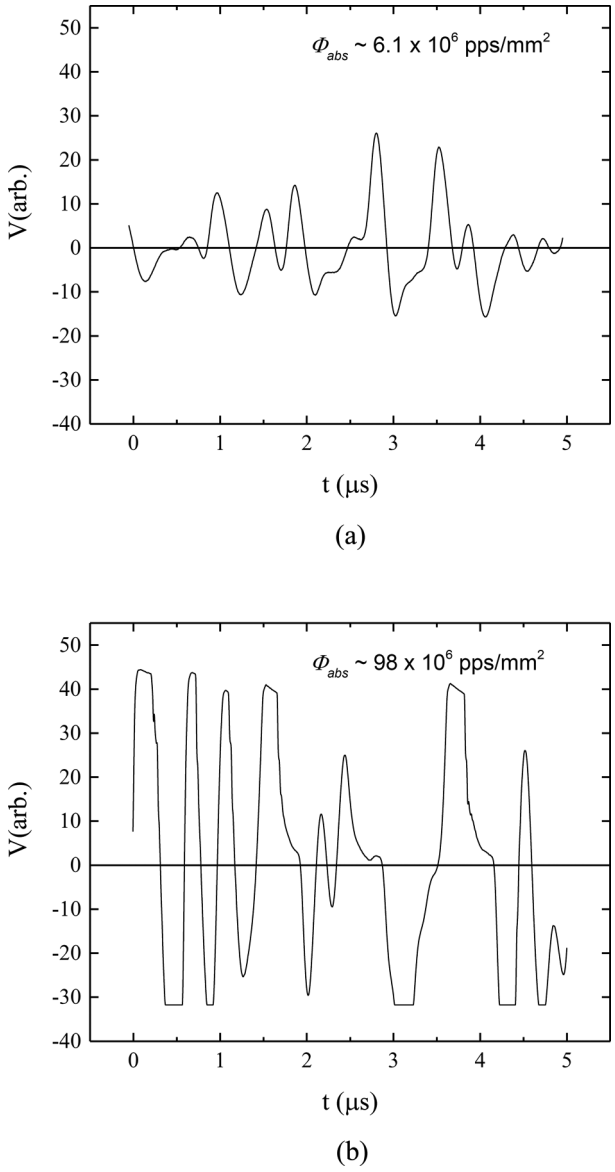

Fig. 6. Sequences of pulses recorded from the bipolar shaper output at (a) ~ 6 Mil. pps/mm^2 and (b) ~ 100 Mil. pps/mm^2 with a non-polarizing detector connected.

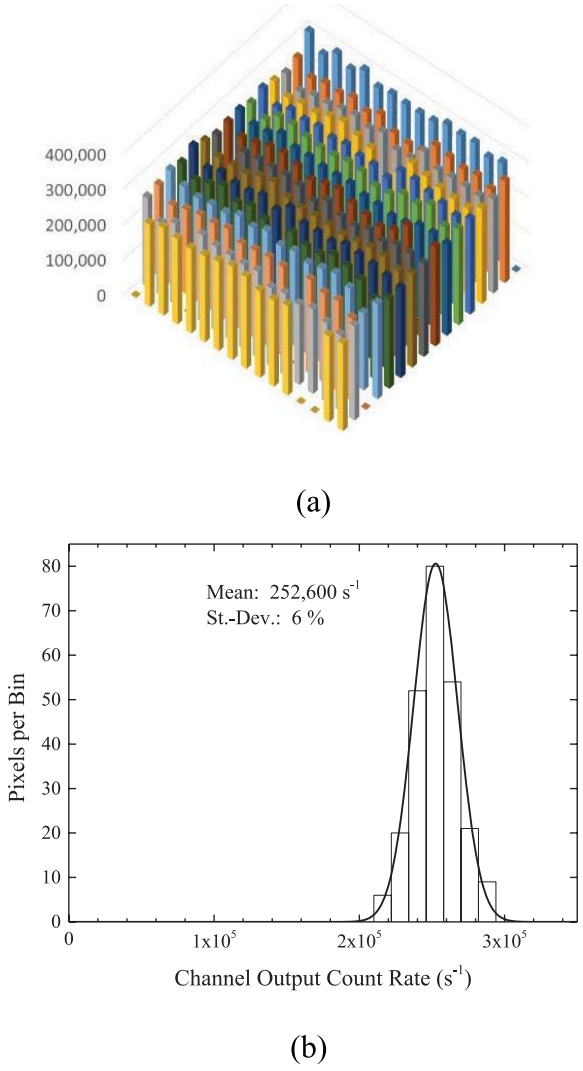

Fig. 7. (a) 2-D map of the channel count rates of all 256 pixels at Φ_{abs} ~ 1 Mil. pps/mm^2, and (b) Corresponding count rate histogram and distribution curve. Dead electronics channels were removed from statistics.

approaches ~30 Mil. pps/mm^2. Further increasing the flux beyond ~50 Mil. pps/mm^2, we observe a slight depression of the saturated average count rate. One possible reason is that τ_{eff} is not strictly a constant but the average width of the pulses becomes affected by the extreme pileup at higher fluxes causing a slight increase of this parameter [19].

For comparison, Fig. 5 also shows the behavior of the polarizing device from Fig. 4 under high flux levels. Data sets for 762 mm (Fig. 4(a)) and 187 mm target-to-detector cathode distance have been stitched together for this plot. The nature of the signals causing the apparent count response at very high fluxes, which was observed on all polarizing detectors, needs more investigation.

Fig. 6 shows sequences of pulses recorded from the bipolar shaper output at ~ 6 Mil · pps/mm^2 and ~ 100 Mil · pps/mm^2 with a non-polarizing detector connected to the front-end circuitry. While pile-up is clearly visible already at the lower flux, the extremely piled up pulses at high flux are completely distorted and the amplitudes get clipped. However, the electronics does not paralyze and the system is still useful to verify non-polarization of the radiation detector.

Note that the energy information is basically lost in this regime and pile up of reduced amplitude signals might still produce enough counts above threshold to saturate the counting electronics. A more detailed study would require the employment of faster counting electronics with energy binning capability and a modified device design to ensure the separation of the charge pulses itself. This can involve thinner devices and smaller pixels but while those approaches can help materials characterization, they are not necessarily an option for imaging applications due to compromises in efficiency and image contrast. Alternatively, the analyses could be done by complete elimination of signal shaping circuitry, i.e., direct evaluation of charge sensitive or trans-impedance preamplifier output.

VII. Count Rate Uniformity

The actual count rate distribution of all 256 pixels can be evaluated at lower fluxes where the output count rate is not significantly pile-up distorted. Fig. 7 shows the analysis for $\Phi_{abs} \sim 1$ Mil. pps/mm^2, which corresponds to the lowest flux in Fig. 3 (same detector). The standard deviation of the nearly Gaussian channel count rate distribution is $\pm 6\%$ for this detector. In general, the THM-CZT detectors from the ingots investigated so far are typically more uniform than what we observed previously from high-flux capable HP-EDG grown material [18].

Note that those pixel-to-pixel count rate variations can be easily corrected for as long as they are not flux dependent, e.g., dynamic lensing [20].

VIII. Summary

We developed a THM-based CZT crystal growth technology to support high-flux x-ray photon counting applications. We verified that 3 mm thick monolythic array detectors fabricated from those ingots can be operated at $\sim$100 Mil. pps/mm^2 at room temperature without polarizing. The ASICs used in this study were relatively slow and a non-paralyzable counting model, based on $\sim$ 600 ns resolution time, perfectly describes the output count rates of the signal chains connected to the 0.25 mm^2 anode pixels until saturation at an absorbed flux of $\sim$ 30 Mil. pps/mm^2. While no quantitative analysis can be achieved with this test configuration beyond that point, we demonstrate that the test system is still sufficient for CZT materials evaluation up to the highest fluxes we could apply, i.e., $\sim$100 Mil. pps/mm^2.

References

[1] J. P. Schlomka, E. Roessl, R. Dorscheid, S. Dill, G. Martens, T. Istel, C. Bäumer, C. Herrmann, R. Steadman, G. Zeitler, A. Livne, and R. Proksa, "Experimental feasibility of multi-energy photon-counting K-edge imaging in pre-clinical computed tomography," *Phys. Med. Biol.*, vol. 53, pp. 4031–4047, 2008.

[2] P. M. Shikhaliev, "Energy-resolved computed tomography: first experimental results," *Phys. Med. Biol.*, vol. 53, pp. 5595–6613, 2008.

[3] J. S. Iwanczyk, E. Nyg˚ard, O. Meirav, J. Arenson, W. C. Barber, N. E. Hartsough, N. Malakhov, and J. C. Wessel, "Photon counting energy dispersive detector arrays for x-ray imaging," *IEEE Trans. Nucl. Sci.*, vol. 56, pp. 535–542, 2009.

[4] K. Taguchi and J. S. Iwanczyk, "Vision 20/20: single photon counting x-ray detectors in medical imaging," *Med. Phys.*, vol. 40, p. 100901_1-19, 2013.

[5] P. M. Shikhaliev, "Medical x-ray and CT imaging with photon-counting detectors," in *Radiation Detectors for Medical Imaging*. Boca Raton, FL, USA: CRC Press, 2015, pp. 47–80.

[6] I. Blevis and R. Levinson, "Photon-counting detectors and clinical applications in medical CT imaging," in *Radiation Detectors for Medical Imaging*. Boca Raton, FL, USA: CRC Press, 2015, pp. 169–192.

[7] W. C. Barber, J. C. Wessel, E. Nyg˚ard, and J. S. Iwanczyk, "Energy dispersive CdTe and CdZnTe detectors for spectral clinical CT and NDT applications," *Nucl. Instrum. and Methods Phys. Res. A*, vol. 784, pp. 521–537, 2015.

[8] C. Szeles, S. E. Cameron, S. A. Soldner, J.-O. Ndap, and M. D. Reed, "Development of the high-pressure electro-dynamic gradient crystal-growth technology for semi-insulating CdZnTe growth for radiation detector applications," *J. Electron. Mater.*, vol. 33, pp. 742–751, 2004.

[9] H. Chen, S. A. Awadalla, J. Mackenzie, R. Redden, G. Bindley, A. E. Bolotnikov, G. S. Camarda, G. Carini, and R. B. James, "Characterization of traveling heater method (THM) grown $Cd_{0.9}Zn_{0.1}Te$ crystals," *IEEE Trans. Nucl. Sci.*, vol. 54, pp. 811–816, 2007.

[10] H. Shiraki, M. Funaki, Y. Ando, A. Tachibana, S. Kominami, and R. Ohno, "THM growth and characterization of 100 mm diameter CdTe single crystals," *IEEE Trans. Nucl. Sci.*, vol. 54, pp. 117–1723, 2009.

[11] R. Triboulet, "CdTe and CdZnTe growth," in *CdTe and Related Compounds: Physics, Defects, Hetero- and Nano-structures, Crystal Growth, Surfaces and Applicant*. Amsterdam, The Netherlands: Elsevier, 2009, pp. 19–73.

[12] M. Prokesch, "CdZnTe for gamma and x-ray applications," in *Solid-State Radiation Detectors: Technol. and Applicant*. Boca Raton: CRC Press, 2015, pp. 17–48.

[13] D. S. Bale and C. Szeles, "Nature of polarization in wide-bandgap semiconductor detectors under high-flux irradiation: Application to semi-insulating $Cd_{1-x}Zn_xTe$," *Phys. Rev. B*, vol. 77, pp. 35205_1–16, 2008.

[14] G. Prekas, P. J. Sellin, P. Veeramani, A. W. Davies, A. Lohstroh, M. E. Özsan, and M. C. Veale, "Investigation of the internal electric field distribution under in situ x-ray irradiation and under low temperature conditions by the means of the pockels effect," *J. Phys. D*, vol. 43, pp. 085102_1–6, 2010.

[15] P. J. Sellin, G. Prekas, J. Franc, and R. Grill, "Electric field distributions in CdZnTe due to reduced temperature and x-ray irradiation," *Appl. Phys. Lett.*, vol. 96, pp. 133509_1–3, 2010.

[16] K. Okada, Y. Sakurai, and H. Suematsu, "Characteristics of both carriers with polarization in diode-type CdTe x-ray detectors," *Appl. Phys. Lett.*, vol. 90, pp. 063504_1–3, 2007.

[17] A. Cola and I. Farella, "The polarization mechanism in CdTe schottky detectors," *Appl. Phys. Lett.*, vol. 94, pp. 102113_1–3, 2009.

[18] C. Szeles, S. A. Soldner, S. Vydrin, J. Graves, and D. S. Bale, "Ultra high flux 2D CdZnTe monolithic detector arrays for x-ray imaging applications," *IEEE Trans. Nucl. Sci.*, vol. 54, pp. 1350–1358, 2007.

[19] C. Szeles, S. A. Soldner, S. Vydrin, J. Graves, and D. S. Bale, "CdZnTe semiconductor detectors for spectroscopic x-ray imaging," *IEEE Trans. Nucl. Sci.*, vol. 55, pp. 572–582, 2008.

[20] S. A. Soldner, D. S. Bale, and C. Szeles, "Dynamic lateral polarization in CdZnTe under high flux x-ray irradiation," *IEEE Trans. Nucl. Sci.*, vol. 54, pp. 1723–1727, 2007.